A Novel Design on the 12-DOF Force and Acceleration Sensing

Fenglei Ni *[1], Tian Zou [2], Kui Li [3], Yongjun Sun[4], Hong Liu[5]

*1 *State Key Laboratory of Robotics and System (HIT), Harbin, China. E-mail: Flni@hit.edu.cn*

ABSTRACT

To resist residual vibration of end effectors, achieve sophisticated tasks with better tracking performance, a novel 12-DOF sensor is developed, which possesses compactness, shock resistance and easy-to-integrate properties. The sensor is constituted by a six-axis force/torque module, a six-axis acceleration module and an acquisition board. The force/torque module is proposed on the basis of the strain stress principle, and the acceleration module is based on the free motion of the generic rigid body in the inertial reference frame. The parameters calibration and signal processing of 12-DOF sensor are proposed for improving the performance of manipulator controllers. After being calibrated, the force measuring accuracy is 1.48%, torque measuring precision is 1.34%, and relative measurement errors of gravity acceleration is decreased from 5.18% to 1.68%. Experimental results demonstrate the effectiveness of the 12-DOF sensor in practice.

1 INTRODUCTION

Higher tracking performance with better motion stability of the space manipulator is critical for numerous space tasks, such as orbital replacement units (ORUs) operations and astronaut assistance. That the fusion of six degrees of freedom (6-DOF) force/torque (F/T) information and 6-DOF accelerations achieves the following diverse applications: (1) the extraction of contact force in ORUs replacement fulfilling the preclusion of inertial force; (2) estimation of all the inertial parameters of load; (3) vibration suppression of end effectors; (4) acceleration controller in Cartesian coordinate frame by the feedback of 6-DOF acceleration [1-3]. In the past several decades, 12-DOF sensor has been absorbing popular concerns, whereas few papers and prototypes are in public. In 2011, a 12-DOF sensor is equipped on the SSRMS in the STS-121 flight mission. By now, there are no open literatures related to the application of 6-DOF accelerations. Lots of scholars concentrates on the 6-DOF F/T sensor only, and there are various F/T sensors based on the strain-stress mechanism in applications which are manufactured by JR3 and ATI. The accurate measurement of 6-DOF accelerations is still a challenge. The allocation of tri-axes gyroscopes and multiple linear accelerometers accomplished the measurement of 6-DOF accelerations indeed, whereas the application is blocked by the disadvantages of gyroscopes including the slow response time, low precision and short durability. Other physical phenomena were adopted to achieve the measurement of 6-DOF accelerations, common disadvantages are difficult-to-fabricate and cross-talking among different degrees. In [4-6], it is demonstrated that these sensors based on multiple linear accelerometers only achieved better performance than that fulfilled by low cost gyroscopes. In [7], Naseri argued that the gyro-free sensors would be the common IMUs in future.

To restrain the residual vibration of end effectors, identify all the inertial parameters of the load and improve the elasticity of collision, a new 12-DOF force/torque and acceleration sensor is presented. The sensor consists of the 6-DOF F/T module, the 6-DOF accelerations module and an acquisition board. The six-axis force/torque module is designed on the basis of the strain stress principle. Linear deformation zones are analyzed in detail for the adhesion of strain gauges. Stud protection is utilized to avoid overload. Besides, according to the kinematics of the rigid body moving freely, a novel spatial configuration is submitted, which achieves the measurement of 6-DOF accelerations. The advantages are compactness, shock resistance, easy-to-integrate, rapid response and durability, etc.

2 STRUCTURE DEVELOPMENT OF 12-DOF SENSOR

2.1 Framework of the 12-DOF Sensor

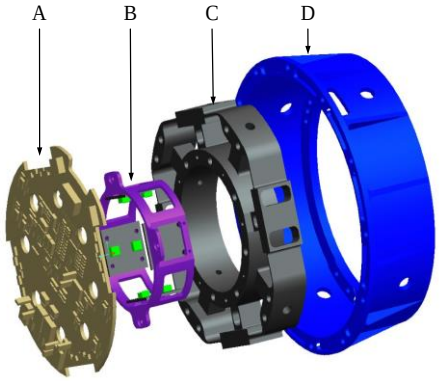

Figure 1: Structure of the 12-DOF sensor

The explosive 3D model of the 12-DOF sensor is shown in Figure 1. Letters A, B, C and D are acquisition board, acceleration module, F/T module and shell of the sensor. The acquisition board is to sample all sensor data and communicate with the host computer. There are eight dual-axes linear accelerometers distributed equally on four printed circuit boards (PCBs). These four PCBs are fixed on a frame every $\pi/2$ rad. The 6-DOF acceleration module is attached on the inner rim of six-axis F/T module.

2.2 Structural Development of Force Module

The measurement of 6-DOF F/T is achieved based on

the strain stress principle. The 3D model and finite element analysis of the elastic body for 6-DOF F/T measurement, which is constituted by the inner beam B_1, outer beam B_2, rim B_3, connecting plate B_4 and hub B_5, as is shown in Figure 2. The inner beam B_1 and outer beam B_2 constitute a T-beam with three through-holes. The coordinate system of the F/T module is fixed on the geometric center of elastic body. The center axis of hub B_5 coincides with z-axis. The x-axis is perpendicular to z-axis and parallels the inner beam B_2. Then, the y-axis is determined by right-handed formula. The inner beam B_1 is used to measure *Fx*, *Fy*, and *Mz*, the outer beam B_2 is used to measure the *Fz*, *Mx* and *My*. Where $F_\cdot$ and $M_\cdot$ are the sensed force and torque.

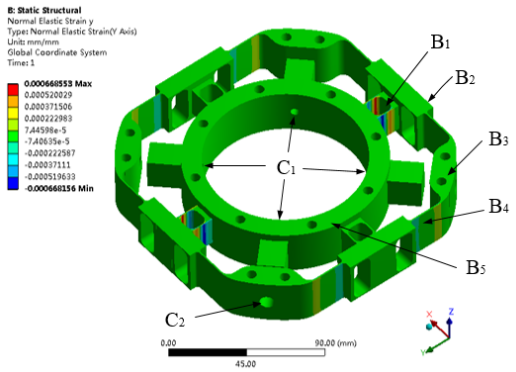

Figure 2: Finite element analysis of the elastic body

To avoid being damaged arising from overload, four dowels and holes labeled by C_1 are designated. The corresponding holes indicated by C_2 in B_3 match with the dowels by clearance fit. The clearance value is predetermined by overload capacity of the elastic body, which could be accurately obtained by finite element analysis method (FEA). The results of FEA is indicated in Figure 2, if only the force along x-axis is applied to the elastic body.

2.3 Develop of Acceleration Module

According to the kinematics of the free rigid body moving in Cartesian space, the generic output a_i of a single accelerometer is derived as follows [6].

$$a_i = u_i^T \ddot{p}_i = \begin{bmatrix} u_i^T & -u_i^T R_i \end{bmatrix} \begin{bmatrix} \ddot{p}_b + g \\ \dot{w}_b \end{bmatrix} + u_i^T \Omega_b^2 r_i \quad (1)$$

Where $r_i=[r_{ix}\ r_{iy}\ r_{iz}]^T$ and $u_i=[u_{ix}\ u_{iy}\ u_{iz}]^T$ are the position vector and orientation vector of a linear accelerometers presented in the sensor frame, respectively. $R_i=(r_i\times)\in\mathbb{R}^{3\times3}$ and $\Omega_b=(w_b\times)\in\mathbb{R}^{3\times3}$ are skew matrices of r_i and w_b, where $w_b=[w_{bx}\ w_{by}\ w_{bz}]^T$ is the angular velocity of the rigid body in inertial frame (IF). $\ddot{p}_b + g$ and $\dot{w}_b$ are the 3-DOF linear and angular acceleration described in IF.

According to equation(1), at least six linear accelerometers are claimed for the measurement of 6 DOF accelerations. If N linear accelerometers are utilized, the sensing equation of all linear accelerometers can be written as

$$\begin{bmatrix} a_1 \\ \vdots \\ a_N \end{bmatrix} = \begin{bmatrix} J_1^T & J_2^T \end{bmatrix} \begin{bmatrix} \ddot{p}_b + g \\ \dot{w}_b \end{bmatrix} + \begin{bmatrix} u_1^T \Omega_b^2 r_1 \\ \vdots \\ u_2^T \Omega_b^2 r_2 \end{bmatrix}$$

$$J_1 = \begin{bmatrix} u_1 & u_2 & \cdots & u_N \end{bmatrix} \quad (2)$$

$$J_2 = \begin{bmatrix} -R_1^T u_1 & -R_2^T u_2 & \cdots & -R_N^T u_N \end{bmatrix}$$

Based on the above analysis, a novel spatial geometric configuration for the measurement of 6-DOF acceleration is proposed, which is shown in Figure 3. There are eight dual-axis accelerometers distributed cylindrically. The radius of the distribution cycle is R and the height of the cylinder is L. The coordinate system for the measurement of 6-DOF acceleration coincide with that for the 6-DOF F/T measurement. The radius and height of the distribution cylinder are 35mm and 20mm, respectively. According to the proposed configuration, the module of 6-DOF acceleration is constituted by a housing frame and four circuit boards. Each circuit board is equipped with two dual-axis accelerometers. The accelerometers utilized are the ADIS16006 manufactured by the Analogy Devices, they are the MEMS accelerometers based on the capacitor principle. When the motion state changes, the inner capacitor varies with the relative displacement of the capacitor plate. Then the varying signal accesses to the AD converter after the signal tuning.

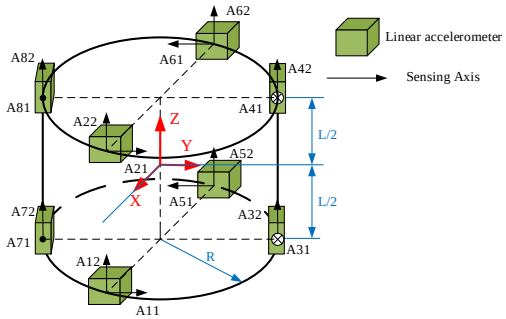

Figure 3: Spatial arrangement of accelerometers

For simplification, both orientation and position inaccuracy are precluded. The position vector and the direction cosine matrix of all linear accelerometers are written as follows.

$$r_i = \begin{bmatrix} R & R & R & R & 0 & 0 & 0 & 0 & -R & -R & -R & -R & 0 & 0 & 0 & 0 \\ 0 & 0 & 0 & 0 & R & R & R & R & 0 & 0 & 0 & 0 & -R & -R & -R & -R \\ -\frac{L}{2} & -\frac{L}{2} & \frac{L}{2} & \frac{L}{2} & -\frac{L}{2} & -\frac{L}{2} & \frac{L}{2} & \frac{L}{2} & -\frac{L}{2} & -\frac{L}{2} & \frac{L}{2} & \frac{L}{2} & -\frac{L}{2} & -\frac{L}{2} & \frac{L}{2} & \frac{L}{2} \end{bmatrix} \quad (3)$$

$$u_i = \begin{bmatrix} 0 & 0 & 0 & 0 & -1 & 0 & -1 & 0 & 0 & 0 & 0 & 0 & 1 & 0 & 1 & 0 \\ 1 & 0 & 1 & 0 & 0 & 0 & 0 & 0 & -1 & 0 & -1 & 0 & 0 & 0 & 0 & 0 \\ 0 & 1 & 0 & 1 & 0 & 1 & 0 & 1 & 0 & 1 & 0 & 1 & 0 & 1 & 0 & 1 \end{bmatrix} \quad (4)$$

According to the equation(2), we can get the following decoupling matrix by the generic inverse matrix method.

$$\begin{bmatrix} \ddot{p}_{bx} \\ \ddot{p}_{by} \\ \ddot{p}_{bz} \\ \dot{w}_{bx} \\ \dot{w}_{by} \\ \dot{w}_{bz} \end{bmatrix} = \begin{bmatrix} 0 & 0 & 0 & 0 & -\frac{1}{4} & 0 & -\frac{1}{4} & 0 & 0 & 0 & 0 & 0 & \frac{1}{4} & 0 & \frac{1}{4} & 0 \\ \frac{1}{4} & 0 & \frac{1}{4} & 0 & 0 & 0 & 0 & 0 & -\frac{1}{4} & 0 & -\frac{1}{4} & 0 & 0 & 0 & 0 & 0 \\ 0 & \frac{1}{8} & 0 & \frac{1}{8} & 0 & \frac{1}{8} & 0 & \frac{1}{8} & 0 & \frac{1}{8} & 0 & \frac{1}{8} & 0 & \frac{1}{8} & 0 & \frac{1}{8} \\ \frac{1}{4L} & 0 & -\frac{1}{4L} & 0 & 0 & \frac{1}{8R} & 0 & \frac{1}{8R} & -\frac{1}{4L} & 0 & \frac{1}{4L} & 0 & 0 & -\frac{1}{8R} & 0 & -\frac{1}{8R} \\ 0 & -\frac{1}{8R} & 0 & -\frac{1}{8R} & \frac{1}{4L} & 0 & -\frac{1}{4L} & 0 & 0 & \frac{1}{8R} & 0 & \frac{1}{8R} & -\frac{1}{4L} & 0 & \frac{1}{4L} & 0 \\ \frac{1}{8R} & 0 & \frac{1}{8R} & 0 & \frac{1}{8R} & 0 & \frac{1}{8R} & 0 & \frac{1}{8R} & 0 & \frac{1}{8R} & 0 & \frac{1}{8R} & 0 & \frac{1}{8R} & 0 \end{bmatrix} \begin{bmatrix} A_{11} \\ A_{12} \\ . \\ . \\ . \\ A_{81} \\ A_{82} \end{bmatrix} \quad (5)$$

3 SIGNAL TUNING OF 12-DOF SENSOR

3.1 System Framework

The system framework is shown in Figure 4. The host computer is utilized to achieve the following functions: (1) control of the 12-DOF sensor; (2) fusion of sensor information; (3) error compensation of the 12-DOF sensor; (4) graphic display of 12-DOF information. A Field Programmable Gate Array (FPGA) is adopted in the acquisition board, which is used to acquire all sensor data and communicate with the host computer. All codes are developed by hardware programming language. A dedicated software timer is utilized to synchronize all clocks and control the sampling procedures. Default sampling time is 10ms. The communication is achieved by the Universal Asynchronous Receiver/Transmitter (UART). Initialized baud rate is 115.2kbps, it can be reset according to our desire. Digital crystal technology is utilized to generate the clock for baud rate. The advantage is that the precision of clock increases with the increase of baud rate.

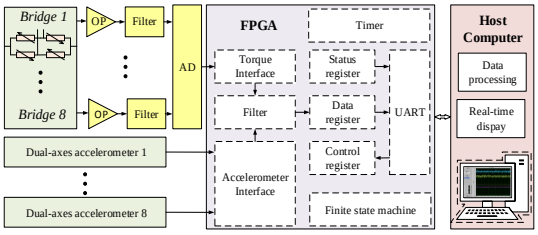

Figure 4: System framework

3.2 Conditioning of 6-DOF F/T

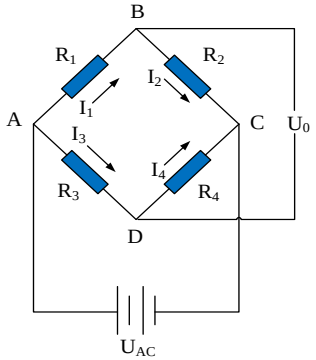

Figure 5: Wheatstone bridge

For each F/T sensing direction, there are four strain gauges, which are used to constitute the Wheatstone bridge, as is shown in Figure 5. The output voltage of the Wheatstone bridge is as follows.

$$U_0 = U_{AC} K \varepsilon_d \quad (6)$$

Where U_{AC}, K and ε_d are the applied voltage, strain coefficient and deformation of strain gauge, respectively. The 8 full Wheatstone bridges which are composed by 32 foil gage are used to measure *Fx* (one bridge), *Fy* (one bridge), *Fz* (two bridges), *Mx* (one bridge), *My* (one bridge), *Mz* (two bridges) respectively. The output voltage of each Wheatstone bridge is amplified by instrumental operation amplifier (OP), which is setup by three OPs. The enlarged signal varies in the range from 0.5V to 4.5V. A Butterworth low-pass filter is adopted to constrain the noises, which is also composed by OPs. The OP is TLV2462 manufactured by Texas Instruments (TI) with rain-to-rail input/output property. Finally, the conditioned signal is numbered by an AD converter.

3.3 Conditioning of 6-DOF Acceleration

The acceleration errors can be divided into the following three parts in this paper:

a) Output error of the linear accelerometer, including amplification factor *k* and static bias *b*;
b) Installation error of the linear accelerometer, including the position error Δr and orientation error Δu;
c) Random error *w* of the linear accelerometer.

The first two categories are definite error, and they can be calibrated by experiments and be omitted by the predefined strategies [8]. The last error can only be furnished by some filter technologies such as Kalman filters [9], multi-rate and multi-resolution filters [10], etc. The Kalman Filter is an optimal state estimation method that can be applied to the dynamic system with random interference. Specifically, the Kalman Filter gives a recursive algorithm, which is a linear unbiased optimal estimation, depending on the real time data we acquire that contaminated by noise. The algorithm has been widely used in many fields of industrial control, such as video and laser tracking system, satellite navigation, ballistic missile trajectory estimation, radar and fire control etc. The Kalman Filter is adopted based on the model of 6-DOF acceleration in equation(5).

For the stochastic system in this paper, the state vector can be presented by

$$X = \begin{bmatrix} x_1 & x_2 \end{bmatrix}^T$$
$$x_1 = \begin{bmatrix} \dot{p}_x & \dot{p}_y & \dot{p}_z & w_x & w_y & w_z \end{bmatrix}^T \quad (7)$$
$$x_2 = \begin{bmatrix} \ddot{p}_{bx} & \ddot{p}_{by} & \ddot{p}_{bz} & \dot{w}_{bx} & \dot{w}_{by} & \dot{w}_{bz} \end{bmatrix}^T$$

Where, x_1 and x_2 are the generalized velocity and acceleration, respectively. The first three terms in x_1 and x_2 are related to translational motion and the last three terms are identified with the rotation. The equation (2) indicates that the observation matrix of Kalman filter is nonlinear. Consequently, Extended Kalman Filter (EKF) is be applied and the system model is as follows.

$$X(k+1) = AX(k) + FW(k)$$
$$Z(k) = f_k[X(k)] + V(k) \quad (8)$$
$$A = \begin{bmatrix} I_6 & T_6 \\ 0_6 & I_6 \end{bmatrix} \quad F = \begin{bmatrix} 0_6 & \\ & T_6 \end{bmatrix}$$

System noise and observation noise are indicated by W and V, and their variance can be presented by Q and R. The EKF algorithm are as follows.

$$\begin{cases} k = 0,1,\cdots \\ \hat{x}_{0|0} = E(x_0) \\ P_{0|0} = Var(x_0) \\ \hat{x}_{k|k-1} = A\hat{x}_{k-1|k-1} \\ P_{k|k-1} = AP_{k-1|k-1}A^T + FQ_{k-1}F^T \\ G_k = P_{k|k-1}H^T\left(HP_{k|k-1}H^T + R_{k-1}\right)^{-1} \\ \hat{x}_{k|k} = \hat{x}_{k-1|k-1} + G_k\left(u_k - H\hat{x}_{k|k-1}\right) \\ P_{k|k} = \left(I - G_k H\right)P_{k|k-1} \end{cases} \quad (9)$$

Where T is the sample time, H can be derived by equation (6).

$$H_k = \begin{pmatrix} \frac{\partial f_1}{\partial x_1} & \frac{\partial f_1}{\partial x_2} & \cdots & \frac{\partial f_1}{\partial x_{12}} \\ \vdots & \vdots & \ddots & \vdots \\ \frac{\partial f_{16}}{\partial x_1} & \frac{\partial f_{16}}{\partial x_2} & \cdots & \frac{\partial f_{16}}{\partial x_{12}} \end{pmatrix} \quad (10)$$

4 Experiment OF THE 12-DOF SENSOR

4.2 Setup of Experimental Platform

There are two diverse experimental platforms are shown in Figure 6. The platform in the Figure 6 a) is F/T calibration platform. Letter *A, B, C, D* are the host computer, power, test bed and loading platform respectively. Figure 6 b) indicates the sketch that the torque around z-axis applied to the sensor. Some identical weights are utilized to achieve different loading. The calibration platform of acceleration is in Figure 6 c), the platform is coupled with a disk by a cylinder appended on the disk. The disk is driven by servo motor. If the disk rotates, the locus projection of the cylinder onto x-axis is sinusoidal typically. There are four different motion modes, which are not given in this paper.

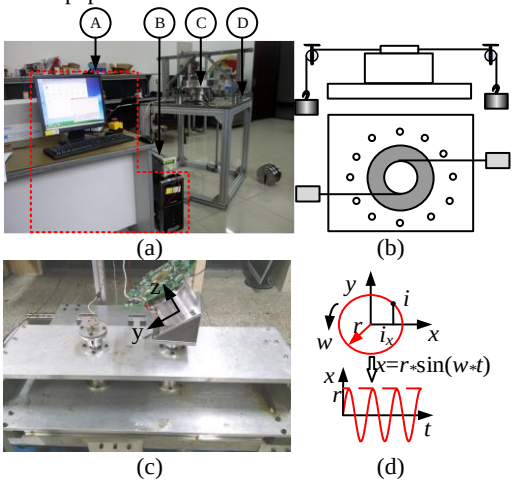

Figure 6: Experimental platform setup

4.1 Calibration of Force Module

In this paper, two different loading mode is adopted, one is the separate loading at every orientation, and the other mode is to achieve loading circumferentially. Both different experimental results are shown in *Figure 7*. The first subfigure is the calibrated results of Mz, which demonstrates the little cross-coupling among different dimensions. The second subfigure is the results of Fy and Fz obtained by the circumferentially loading. The black solid line indicates the results of Fy, and the red dashed line shows the results of Fz.

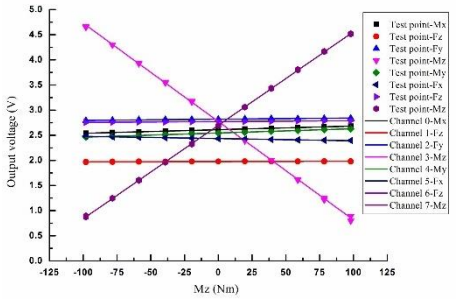

a): Mz Calibration resluts

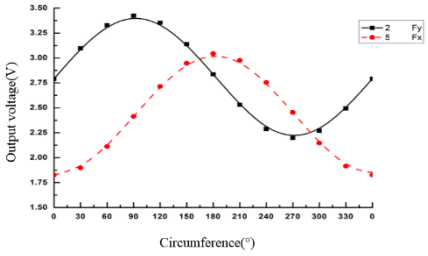

b) Circumferentially loading Verification

Figure 7: Experimental Verification of F/T

The coupling matrix of F/T is derived as follows.

$$F = AV + B \quad (11)$$

Where A and B are written as

$$A=\begin{bmatrix} -350.0962 & -11.1922 & 22.3967 & -0.3791 & -0.2514 & 0.9250 \\ -10.5612 & 347.7417 & -23.8059 & -0.3629 & -0.1840 & 0.2000 \\ -7.7245 & 8.5422 & 580.7237 & -4.5961 & -4.5961 & 0.3637 \\ -2.0359 & 4.0974 & 54.3981 & 55.2445 & -2.246 & 0.0966 \\ -3.3244 & -1.1910 & -62.7235 & -0.5416 & 54.7197 & 0.1036 \\ 19.4673 & 2.7639 & -8.1704 & -0.6556 & 2.9108 & -26.9241 \\ -7.3925 & 2.6757 & -590.9561 & -3.6990 & -3.4611 & 0.2863 \\ 12.6797 & -1.8847 & 3.3757 & -2.7611 & 0.6924 & 25.4568 \end{bmatrix}$$

$$B=\begin{bmatrix} 0.0346 & 10.2426 & -18.3749 & 15.6640 & -2.3156 & 10.2426 \end{bmatrix}^T$$

4.2 Calibration of Acceleration Module

From the aforementioned errors analysis, these parameters involvement are the proportionality coefficient *k*, static bias *b*, installation position vector *r* and the direction vector *u*. The parameters *b*, *k* are related to the linear accelerometers, and the rest ones are demonstrated by the spatial arrangement of the linear accelerometers. The calibration procedure is given in Figure 8. For the static calibrations, the rolling experiments in gravity field are undertaken, which the static bias can be obtained. The other parameters are calibrated on the test bed which is shown in Figure 6 c).

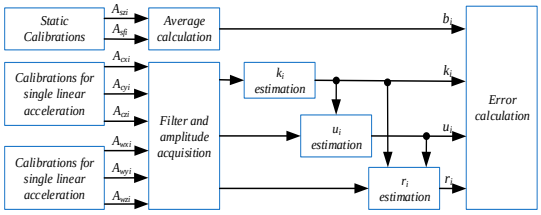

Figure 8: Estimation principle of the accelerometer

Take A_{11} and A_{12} for example, the calibrated results are shown in Table 1. All calibrated errors are then calculated to achieve the direct error compensation.

Table 1: Parameters estimation results

Acc. index	A_{11}	A_{12}
b_i	-0.0657	-0.3853
k_i	0.9908	0.9896
u_i	[0.0017 0.9998 0.0186]^T	[0 0 1]T
r_i	[0.0344 -0.0008 0.0005]^T	[0.0344 -0.0008 0.0005]T

In order to verify the feasibility of error compensation and EKF, the sensor is laid horizontally, and the z-axis of the 12-DOF sensor is vertical. Experimental results of 6-DOF acceleration are shown in Figure 9. The cyan solid line indicates the results derived by the raw information of linear accelerometers. The red dashed line is the results after being compensated. Results proceeded by the proposed algorithm are shown by the blue solid line.

The mean value and variance of 6-DOF acceleration derived by the raw information of linear accelerometers are:

$$a_0=\begin{bmatrix}-0.0001 & 0.0004 & 9.8073 & 0.0064 & -0.0028 & 0.0134\end{bmatrix}^T$$

$$\mathrm{var}_0=\begin{bmatrix}0.0204 & 0.0210 & 0.0296 & 0.8080 & 0.8512 & 0.2760\end{bmatrix}^T$$

After being filtered and compensated, the mean value and variance of 6-DOF acceleration are:

$$a_c=\begin{bmatrix}-0.0004 & 0.0005 & 9.8089 & 0.0025 & 0.0117 & 0.0058\end{bmatrix}^T$$

$$\mathrm{var}_{kf}=\begin{bmatrix}0.0057 & 0.0054 & 0.0063 & 0.0875 & 0.1261 & 0.0789\end{bmatrix}^T$$

Noises are constrained evidently, which identifies the validity of EKF in the acceleration application.

To verify the dynamic performance of the proposed algorithms for acceleration application. The sensor is set on the test beds by an adopting block with a sloping surface, as is shown in Figure 6 c). The 12-DOF sensor is excited by the composite motion, that is, both translational motion and rotation are applied.

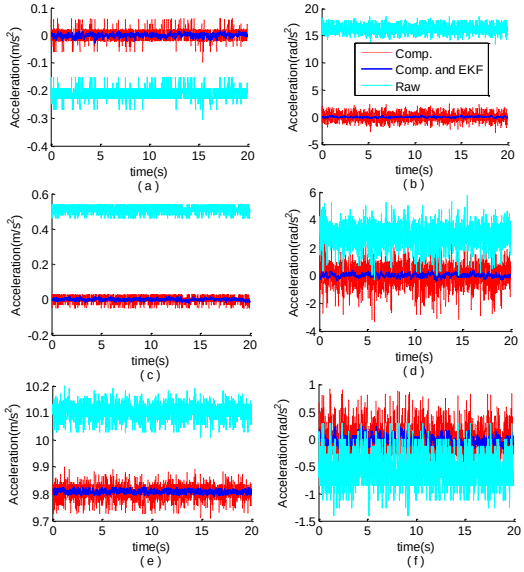

Figure 9: Static output of 6-DOF acceleration

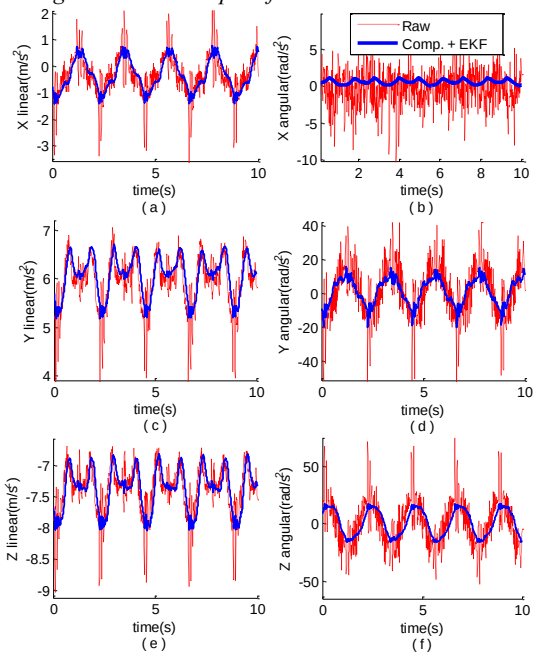

Figure 10: Dynamic output of 6-DOF acceleration

Acceleration results are shown in Figure 10, subfigures labeled by (a), (c) and (e) shows 3-DOF linear acceleration along *x*-axis, *y*-axis and *z*-axis, respectively, and the other three subfigures indicate the angular acceleration around the *x*-axis, *y*-axis and *z*-axis. The red dashed line shows the acceleration without any proceedings, and the blue solid line graphs the results proceeded by the proposed algorithm. Experimental results demonstrate the effectiveness of the 6-DOF acceleration measurement.

5 CONCLUSION

A novel 12-DOF sensor was introduced, which achieved the measurement of 6-DOF F/T and accelerations. Advantages are the compactness, shock resistance and easy-to-integrate properties, etc. Linear deformation zones are investigated in detail for the arrangement of strain gauges, which achieved the measurement of 6-DOF F/T. After being calibrated, the force measuring accuracy was 1.48%, torque measuring precision was 1.34%. A cylindrical configuration was proposed according to the kinematics of a free rigid moving in Cartesian space. Eight dual-axes linear accelerometers were arranged with the reference of the novel cylindrical configuration, fulfilling the measurement of 6-DOF accelerations. Moreover, errors of linear accelerometers are analyzed for the successive error compensation algorithm. The relative measurement errors of gravity acceleration was decreased from 5.18% to 1.68% after being compensated. Experimental results demonstrated the effectiveness of the 12-DOF sensor in practice.

Acknowledgement

This work was supported in part by the National Program on Key Basic Research Project 973 Program under Grant 2013CB733103.

References

[1] Kroger T, Kubus D, Wahl F M. 12d force and acceleration sensing: A helpful experience report on sensor characteristics[C]//Robotics and Automation, 2008. ICRA 2008. IEEE International Conference on. IEEE, 2008: 3455-3462.

[2] Garcia J G, Robertsson A, Ortega J G, et al. Sensor fusion of force and acceleration for robot force control[C]//Intelligent Robots and Systems, 2004.(IROS 2004). Proceedings. 2004 IEEE/RSJ International Conference on. IEEE, 2004, 3: 3009-3014.

[3] Kröger T, Kubus D, Wahl F M. Force and acceleration sensor fusion for compliant manipulation control in 6 degrees of freedom [J]. Advanced Robotics, 2007, 21(14): 1603-1616.

[4] F. Jacob, Handbook of modern sensors: physics, designs, and applications: Springer New York; 2010.

[5] E. Edwan, S. Knedlik, O. Loffeld, Constrained angular motion estimation in a gyro-free IMU, Aerospace and Electronic Systems, IEEE Transactions on, 47(2011) 596-610.

[6] C.-W. Tan, S. Park, Design of accelerometer-based inertial navigation systems, Instrumentation and Measurement, IEEE Transactions on, 54(2005) 2520-30.

[7] H. Naseri, M. Homaeinezhad, Improving measurement quality of a MEMS-based gyro-free inertial navigation system, Sensors and Actuators A: Physical, 207(2014) 10-9.

[8] P. Aggarwal, Z. Syed, X. Niu, N. El-Sheimy, A standard testing and calibration procedure for low cost MEMS inertial sensors and units, Journal of navigation, 61(2008) 323-36.

[9] J. Ali, M. Ushaq, A consistent and robust Kalman filter design for in-motion alignment of inertial navigation system, Measurement, 42(2009) 577-82.

[10] A. Smyth, M. Wu, Multi-rate Kalman filtering for the data fusion of displacement and acceleration response measurements in dynamic system monitoring, Mechanical Systems and Signal Processing, 21(2007) 706-23.